

# Observation of Magnetic Proximity Effect Using Resonant Optical Spectroscopy of an Electrically Tunable MoSe<sub>2</sub>/CrBr<sub>3</sub> Heterostructure

Livio Ciorciaro,<sup>1,\*</sup> Martin Kroner,<sup>1</sup> Kenji Watanabe,<sup>2</sup> Takashi Taniguchi,<sup>2</sup> and Atac Imamoglu<sup>1</sup>

<sup>1</sup>*Institut für Quantenelektronik, ETH Zürich, Auguste-Piccard-Hof 1, 8093 Zürich, Switzerland.*

<sup>2</sup>*National Institute for Materials Science, 1-1 Namiki, Tsukuba 305-0044, Japan*

(Dated: December 15, 2022)

Van der Waals heterostructures combining two-dimensional magnetic and semiconducting layers constitute a promising platform for interfacing magnetism, electronics, and optics. Here, we use resonant optical reflection spectroscopy to observe the magnetic proximity effect in a gate-tunable MoSe<sub>2</sub>/CrBr<sub>3</sub> heterostructure. High quality of the interface leads to a giant zero-field splitting of the K and K' valley excitons in MoSe<sub>2</sub>, equivalent to an external magnetic field of 12 T, with a weak but distinct electric field dependence that hints at potential for electrical control of magnetization. The magnetic proximity effect allows us to use resonant optical spectroscopy to fully characterize the CrBr<sub>3</sub> magnet, determining the easy-axis coercive field, the magnetic anisotropy energy, and critical exponents associated with spin susceptibility and magnetization.

Two-dimensional (2D) magnetic materials have attracted considerable attention due to their potential applications in spintronic devices [1, 2]. Since the first demonstration that magnetism persists down to the monolayer limit in chromium trihalides (CrX<sub>3</sub>, X = Cl, Br, I) [3, 4], much progress has been made, both in understanding fundamental properties of these materials [5–14] and investigation of crucial steps towards applications [15–23]. Concurrently, transition metal dichalcogenides (TMDs) have established themselves as 2D semiconductors with remarkable optical properties [24–26] and possible applications in photonics and valleytronics [27–29]. Van der Waals heterostructures composed of different 2D materials have the potential to realize atomically smooth interfaces that are not affected by lattice structure mismatch between the layers, allowing in principle arbitrary combinations of materials [30]. Magnetic proximity effect in such structures on the one hand leads to transfer of magnetization to otherwise non-magnetic layers, and on the other hand may allow for controlling magnetization using electrical or optical excitation.

In this Letter, we use resonant optical spectroscopy to unequivocally demonstrate the magnetic proximity effect in a MoSe<sub>2</sub>/CrBr<sub>3</sub> heterostructure, where we observe a large zero-field splitting of the K and K' exciton resonances in MoSe<sub>2</sub>. We find that the magnetization of MoSe<sub>2</sub> is exclusively induced by exchange coupling of conduction band electrons. We use the shift of MoSe<sub>2</sub> excitonic resonances to study the magnetic properties of CrBr<sub>3</sub>, and determine the magnetic anisotropy as well as the critical exponents associated with magnetization and susceptibility. Our work establishes resonant optical measurements in heterostructures incorporating TMD monolayers and 2D magnetic materials as a powerful spectroscopic tool that could be invaluable for studying magnetic materials with weak optical transitions without requiring high power laser excitation.

The sample we studied consists of a monolayer MoSe<sub>2</sub> in direct contact with a bilayer CrBr<sub>3</sub> encapsulated in

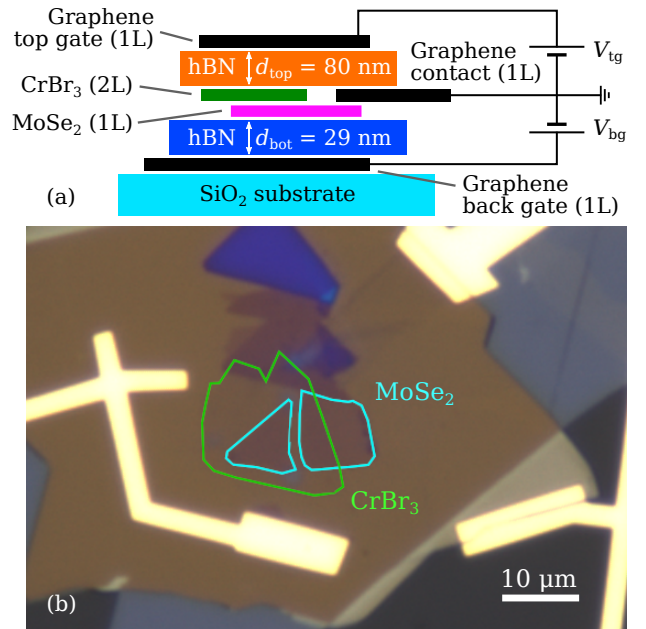


FIG. 1. (a) Schematic of the layer structure of the device and electrical connectivity. A bilayer CrBr<sub>3</sub> and monolayer MoSe<sub>2</sub> are encapsulated in hBN. Monolayer graphene flakes are used as top and bottom gates and as contact to MoSe<sub>2</sub>. The stack is placed on a transparent SiO<sub>2</sub> substrate. (b) Optical micrograph of the device, with MoSe<sub>2</sub> and CrBr<sub>3</sub> outlined in blue and green, respectively.

hexagonal boron nitride (hBN) on a SiO<sub>2</sub> substrate, as shown schematically in Fig. 1(a). In contrast to the layer-antiferromagnets CrI<sub>3</sub> and CrCl<sub>3</sub>, the interlayer exchange in bilayer CrBr<sub>3</sub> has been shown to be ferromagnetic [4]. Monolayer graphene gates and a graphene contact allow for independent tuning of the charge carrier density and out-of-plane electric field in the sample. In the optical micrograph in Fig. 1(b), the regions of bare MoSe<sub>2</sub>, bare CrBr<sub>3</sub>, and the overlapping region can be seen. Details on the sample fabrication, optical setup, and data analy-

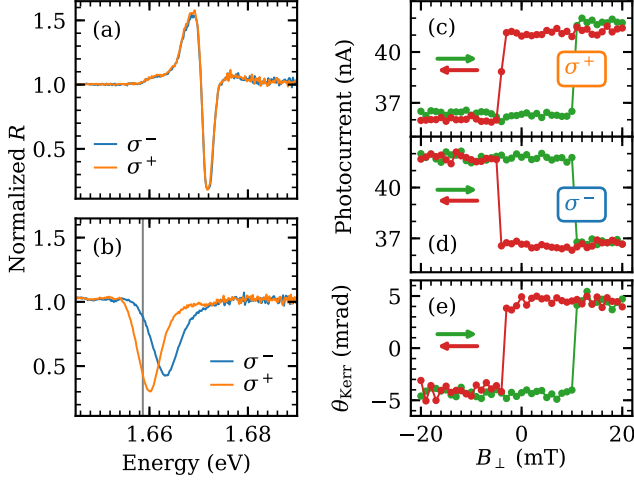


FIG. 2. (a) Reflection spectrum of bare undoped MoSe<sub>2</sub>. (b) Reflection spectra in  $\sigma^-$  and  $\sigma^+$  polarization of the undoped MoSe<sub>2</sub>/CrBr<sub>3</sub> heterostructure at  $B = 0$ . The K and K' valley excitons are split by 2.9 meV. (c), (d) Hysteresis of the reflection of a  $\sigma^+/\sigma^-$  polarized laser tuned to the low-frequency tail of the MoSe<sub>2</sub> exciton in the heterostructure as marked by the vertical line in panel (b). (e) Measurement of the CrBr<sub>3</sub> magnetization hysteresis using the MOKE. The apparent offset from zero of the magnetic field in both measurements is due to a stray field from a ferromagnetic component in the cryostat.

sis are given in the Supplemental Material [31]. All measurements were performed at approximately 6 K unless stated otherwise.

Normalized polarization-resolved reflection spectra of the bare MoSe<sub>2</sub> and the MoSe<sub>2</sub>/CrBr<sub>3</sub> heterostructure are shown in Fig. 2(a) and (b), for a choice of gate voltages that ensure charge neutrality of MoSe<sub>2</sub>. In the absence of an external magnetic field, the K and K' valley excitons are degenerate in bare MoSe<sub>2</sub> and the spectrum shows no polarization dependence. In contrast, a valley splitting of 2.9 meV emerges in the MoSe<sub>2</sub>/CrBr<sub>3</sub> heterostructure region, equivalent to an external magnetic field of 12 T, assuming the electronic g-factor to be 4. This splitting can be attributed to an exchange coupling between electronic states in MoSe<sub>2</sub> and spin-polarized states in CrBr<sub>3</sub> that leads to different energy shifts for the MoSe<sub>2</sub> K and K' valley excitons. Due to strain and disorder in the heterostructure, the splitting varies spatially by approximately 10 %.

To demonstrate that the MoSe<sub>2</sub> exciton valley splitting originates from the magnetization of CrBr<sub>3</sub>, we compare hysteresis measurements of the MoSe<sub>2</sub> reflectance as a function of an external out-of-plane magnetic field  $B_\perp$  to the established method of measuring CrBr<sub>3</sub> magnetization along the easy axis using the magneto-optical Kerr effect (MOKE) [4]. Figures 2(c) and (d) show the reflectance of a right- and left-hand circularly polarized ( $\sigma^+/\sigma^-$ ) laser (5  $\mu$ W CW) tuned to the low-frequency

tail of the exciton resonance, as indicated by the vertical line in Fig. 2(b), as a function of  $B_\perp$ . For this choice of laser detuning, the valley splitting gives rise to maximal contrast in magnetic circular dichroism (MCD). The MOKE depicted in Fig. 2(e) is measured on the same spot with a linearly polarized laser at 2.755 eV (450 nm, 20  $\mu$ W CW). The one-to-one correspondence between the measurements confirms that the valley splitting is directly linked to the magnetization of CrBr<sub>3</sub>. We verified that the MOKE signal is not altered by the presence of MoSe<sub>2</sub> by comparing measurements on the heterostructure and bare CrBr<sub>3</sub> (see Supplemental Material [31]). Using resonant spectroscopy on MoSe<sub>2</sub> instead of the MOKE to access the magnetization of CrBr<sub>3</sub> is advantageous, since it allows us to perform the same measurement with a simpler technique and lower illumination power. Avoiding measurements requiring high laser intensity is particularly important for chromium trihalides where sizeable MOKE signals are only obtained using above-band-gap lasers that could cause heating. Moreover, identifying peak positions instead of measuring laser intensities after a polarizing beam splitter makes our spectroscopic method less sensitive to imperfections in the polarization selection than traditional techniques.

An exchange splitting of similar magnitude has been reported in the pioneering work on photoluminescence (PL) measurements of WSe<sub>2</sub>/CrI<sub>3</sub> heterostructures [5, 14, 20]. We were not able to observe the splitting in PL measurements (see Supplemental Material [31]). Instead, we see broad emission lines with an integrated intensity that is smaller by a factor twenty compared to bare MoSe<sub>2</sub>, which suggests that tunneling to CrBr<sub>3</sub> provides a fast non-radiative relaxation channel for conduction band electrons and excitons in MoSe<sub>2</sub>. Because the exchange coupling responsible for the splitting relies on second-order virtual tunnel coupling, the PL splitting is expected to be large where the tunnel coupling is large, leading to a short exciton lifetime. Since PL primarily originates from long-lived states, we would expect it to be dominated by low-oscillator-strength localized excitations in parts of the heterostructure where the tunnel coupling is small. Consequently, disorder-induced spatial variations of the tunnel coupling could lead to a PL signal that shows small or possibly vanishing exciton valley splitting. This is in contrast to resonant reflection/absorption measurements which probe extended states with high oscillator strength within the optical excitation spot.

To explore the nature of the exchange coupling between CrBr<sub>3</sub> and MoSe<sub>2</sub> we measure the gate voltage dependence of the reflection spectra in  $\sigma^-$  polarization, shown in Fig. 3(a) and (b). The voltages indicated on the vertical axis were applied to both top and bottom gate. The bare MoSe<sub>2</sub> flake can be charged with electrons or holes, evidenced by the appearance of attractive polaron lines at both positive and negative gate voltages

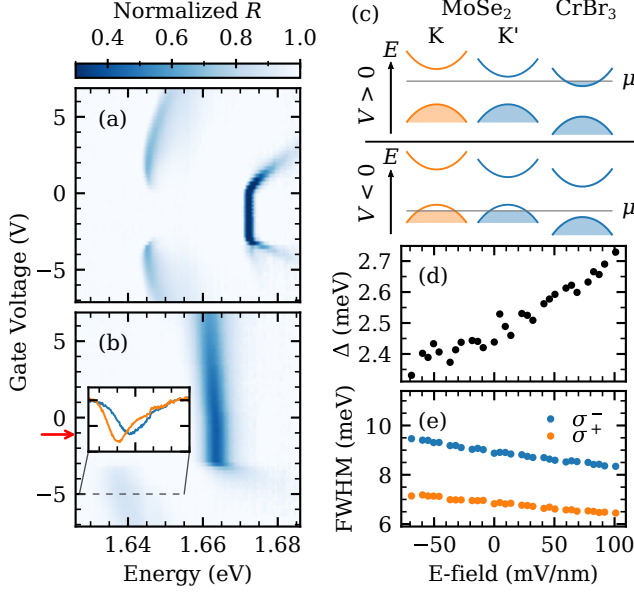


FIG. 3. (a) Gate dependence of the bare MoSe<sub>2</sub> reflection spectrum. The appearance of attractive and repulsive polaron lines at positive and negative voltages shows the flake can be n- and p-doped. (b) Gate dependence of the reflection spectrum of the heterostructure in  $\sigma^-$  polarization. Due to the type-II band alignment, MoSe<sub>2</sub> cannot be n-doped anymore, as signified by the persistence of the exciton line at positive voltages. Inset: Reflection spectra in the p-doped regime, as indicated by the dashed line. The attractive polaron lines show the same splitting as the exciton lines. The x-ticks are identical to the parent axis, the y-tick separation is 0.1. (c) Schematic of the type-II band alignment of MoSe<sub>2</sub> and CrBr<sub>3</sub> with chemical potential  $\mu$  for positive and negative gate voltages. Exchange coupling leads to valley splitting in the conduction band of MoSe<sub>2</sub>. (d), (e) Dependence of the valley splitting  $\Delta$  and FWHM of the exciton lines on the out-of-plane electric field. Both the splitting and FWHM are tunable, indicating a modification of the tunneling rate across the MoSe<sub>2</sub>/CrBr<sub>3</sub> interface.

[32]. In the presence of CrBr<sub>3</sub>, only holes can be injected into MoSe<sub>2</sub>, consistent with the type-II band alignment schematically shown in Fig. 3(c) and predicted from ab initio calculations [33, 34]. Injected electrons accumulate in the lower-lying conduction band of CrBr<sub>3</sub>, leaving the MoSe<sub>2</sub> undoped and leading to screening of the top gate (see Supplemental Material [31]).

The attractive polaron line on the p-doped side exhibits the same valley splitting as the neutral exciton, as shown in the inset of Fig. 3(b). If the itinerant holes in MoSe<sub>2</sub> were subject to a sizeable exchange interaction, we would observe a strong valley polarization of holes, leading to a single circularly polarized attractive polaron resonance [35, 36]. The observation of polaron resonances with equal strength for the two polarizations demonstrates that electron exchange is predominantly responsible for the exciton and polaron valley splitting. A

detailed understanding of the underlying coupling mechanism is beyond the scope of this Letter and requires additional theoretical work.

The presence of top and bottom gates allows us to probe the electric field dependence of the reflectance for constant chemical potential. In the absence of mobile charges in the heterostructure, the electric field is approximately given by  $E \approx (V_{\text{tg}} - V_{\text{bg}}) / (d_{\text{top}} + d_{\text{bot}})$  and the chemical potential by  $\mu \propto d_{\text{bot}} V_{\text{tg}} + d_{\text{top}} V_{\text{bg}}$ , where  $d_{\text{top}}$  and  $d_{\text{bot}}$  are the thicknesses of the top and bottom hBN flakes; the actual electric field may deviate by a constant factor due to the dielectric constants and finite thickness of MoSe<sub>2</sub> and CrBr<sub>3</sub> (see Supplemental Material [31]). To keep the chemical potential constant while varying the electric field, we tune the gate voltages with a fixed ratio  $(V_{\text{tg}} - V_0) / V_{\text{bg}} = 3.3$ , where  $V_0$  determines the chemical potential; we determined this ratio experimentally from 2D gate sweeps (see Supplemental Material [31]).

Figures 3(d) and (e) show the valley splitting and the reflection peak widths, respectively, for the neutral exciton as a function of the applied electric field. The choice of gate voltages, indicated by the red arrow in Fig. 3(b), ensures the charge neutrality of the heterostructure. Clear dependence of both the splitting and the linewidth on the electric field suggests that the tunnel coupling strength is modified. Such an approximately linear electric field dependence of the splitting was predicted in theoretical works [33, 34] and may have implications for future gate-tunable spintronic devices. Additionally, the higher-energy exciton line (here  $\sigma^-$ ) is consistently broader than the lower-energy line, presumably due to the spin-dependent charge transfer between MoSe<sub>2</sub> and CrBr<sub>3</sub>; similar observations were previously reported in heterostructures composed of different 2D magnetic layers [14, 20].

Having demonstrated the magnetic proximity effect in MoSe<sub>2</sub>, we use resonant spectroscopy of the MoSe<sub>2</sub> exciton resonance to determine the magnetic properties of CrBr<sub>3</sub>. Figure 4(a) shows fitted positions of the split exciton peaks as function of an applied in-plane magnetic field  $B_{\parallel}$ . We observe that for  $B_{\parallel} \geq 0.1$  T, the splitting gradually decreases and saturates at a value of 0.1 meV for 0.3 T. The reduction of the splitting is a consequence of the canting of the CrBr<sub>3</sub> spins into the plane. The small remaining splitting at high magnetic fields is due to a tilt of the magnetic field axis with respect to the sample plane that leads to an out-of-plane component of the magnetization and consequently a non-zero exchange field. A striking feature of the data in Fig. 4(a) is the asymmetry in the  $B_{\parallel}$ -induced change in resonance energy between the low- and high-energy exciton peaks: we speculate that this asymmetry could arise from an energy splitting between the spin-polarized conduction bands of CrBr<sub>3</sub> that play a prominent role in determining the exchange coupling to MoSe<sub>2</sub> electrons in different

valleys.

The observed dependence of the splitting vs.  $B_{\parallel}$  allows us to estimate the anisotropy energy of  $\text{CrBr}_3$ . To this end, we assume that the  $\text{CrBr}_3$  flake has a uniform magnetization  $\vec{m}$  and numerically minimize its potential energy  $E = K(\sin\theta)^2 + |m|B_{\parallel}\cos(\theta - \alpha)$ , where  $K$  is the anisotropy energy along the easy axis,  $\theta$  is the angle of the magnetic moment with respect to the easy axis,  $B_{\parallel}$  is the external magnetic field, and  $\alpha$  is the angle of  $B_{\parallel}$  with respect to the easy axis. We set  $|m| = 3.87\mu_B$  to the magnetization per Cr atom [37, 38] and fit the model to the experimental data to obtain an anisotropy energy  $K = 34.3(4)\mu\text{eV}$  per Cr atom and  $\alpha = 88.20(13)^\circ$ . Although this simple model does not tell us anything about the type of anisotropy, previous calculations have shown that it is expected to originate from anisotropic exchange coupling rather than on-site anisotropy [39]. By using the previously reported values of the isotropic intralayer exchange of bulk  $\text{CrBr}_3$  ( $J \approx 0.8\text{ meV}$ ) [40, 41], we find that the exchange interaction is weakly anisotropic,  $J/K \approx 20$ . The small coercive field we measure (Fig. 2(c)–(e)) is consistent with the weak anisotropy of the intralayer exchange interaction. Remarkably, the exciton valley splitting in  $\text{MoSe}_2$  is comparable to the  $\text{CrBr}_3$  intralayer exchange  $J$ , even though the exchange between two  $\text{CrBr}_3$  layers is expected to be significantly smaller [40–42].

Next, we measure the critical temperature  $T_C$  and critical exponents of the second-order magnetic phase transition of  $\text{CrBr}_3$  through resonant  $\text{MoSe}_2$  exciton spectroscopy. To this end, we measure the hysteresis curves of circularly polarized reflection spectra vs.  $B_{\perp}$  as a function of temperature (see Supplemental Material [31]). For  $T < T_C$ , shown in Fig. 4(c), the splitting at  $B_{\perp} = 0$  provides a measure for the remnant magnetization  $m$ , which is the order parameter for the phase transition. For  $T > T_C$ , shown in Fig. 4(d), the slope of the splitting vs.  $B_{\perp}$  is proportional to the magnetic susceptibility  $\chi$ . By fitting the functional forms  $m(T) = A_1(1 - T/T_C)^\beta$  and  $\chi(T) = A_2(T/T_C - 1)^{-\gamma}$  simultaneously to the experimental data, we find the Curie temperature  $T_C = 21.7(3)\text{ K}$  as well as the critical exponents  $\beta = 0.27(3)$  and  $\gamma = 3.1(7)$ . We also perform similar measurements using the MOKE and find that the data points fall onto the same curves when normalized with respect to the peak values of  $m$  and  $\chi$ . The values we obtain for  $\beta$  and  $\gamma$  are consistent with the 2D-Heisenberg model with weak anisotropy [43].

In conclusion, we use resonant exciton reflection measurements of valley splitting in  $\text{MoSe}_2$  to demonstrate a strong magnetic proximity effect due to ferromagnetic  $\text{CrBr}_3$ . From the absence of itinerant hole valley polarization in the reflection spectra we infer that the resulting valley Zeeman effect is predominantly due to exchange coupling between conduction band electrons in  $\text{MoSe}_2$  and  $\text{CrBr}_3$ ; remarkably, the strength of this interlayer ex-

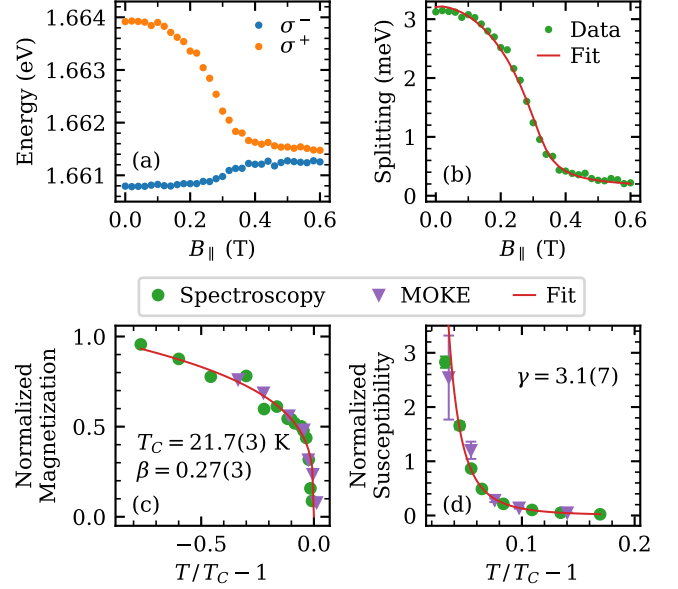


FIG. 4. (a) Fitted exciton peak positions from polarization-resolved reflection spectra as function of in-plane magnetic field. The splitting collapses around 0.3 T, indicating the transition to in-plane magnetization of  $\text{CrBr}_3$ . (b) Exciton valley splitting as function of in-plane magnetic field. The fitted model using a macroscopic magnetic moment with anisotropy is in excellent agreement with the experimental data. (c) Magnetization of  $\text{CrBr}_3$  as function of temperature. Round data points are extracted from polarization-resolved reflection spectra of  $\text{MoSe}_2$  and triangular data points are extracted from MOKE measurements. A fit of the form  $m(T) = A(1 - T/T_C)^\beta$  yields values for the critical temperature  $T_C$  and critical exponent  $\beta$ . (d) Magnetic susceptibility as function of temperature extracted from spectra and MOKE measurements. A fit of the form  $\chi(T) = B(T/T_C - 1)^{-\gamma}$  yields the critical exponent  $\gamma$ .

change coupling is comparable to the intralayer exchange coupling in  $\text{CrBr}_3$ . Our investigation of the magnetic properties of  $\text{CrBr}_3$  using resonant optical spectroscopy reveals several features such as an electric field dependence of the proximity effect, weak anisotropy  $J/K \approx 20$  of the exchange interaction, and the critical exponents associated with the magnetic phase transition.

The data that supports the findings of this Letter is available in the ETH Research Collection [44].

## ACKNOWLEDGMENTS

We gratefully acknowledge the contributions of Alberto Morpurgo and Zhe Wang who introduced us to the field of 2D magnets. Y. Shimazaki and A. Popert contributed to the fabrication of the heterostructure. We also express our gratitude to A. Vindigni and P. Maletinsky for insightful discussions. This work was supported by the Swiss National Science Foundation (SNSF) under Grant



No. 200021-178909/1. K. W. and T. T. acknowledge support from the Elemental Strategy Initiative conducted by the MEXT, Japan, and the CREST (JPMJCR15F3), JST.

---

\* livioc@phys.ethz.ch

- [1] C. Gong and X. Zhang, *Science* **363**, eaav4450 (2019).
- [2] D. L. Cortie, G. L. Causer, K. C. Rule, H. Fritzsche, W. Kreuzpaintner, and F. Klose, *Advanced Functional Materials*, 1901414 (2019).
- [3] B. Huang, G. Clark, E. Navarro-Moratalla, D. R. Klein, R. Cheng, K. L. Seyler, D. Zhong, E. Schmidgall, M. A. McGuire, D. H. Cobden, W. Yao, D. Xiao, P. Jarillo-Herrero, and X. Xu, *Nature* **546**, 270 (2017).
- [4] Z. Zhang, J. Shang, C. Jiang, A. Rasmita, W. Gao, and T. Yu, *Nano Letters* **19**, 3138 (2019).
- [5] D. Zhong, K. L. Seyler, X. Linpeng, R. Cheng, N. Sivadas, B. Huang, E. Schmidgall, T. Taniguchi, K. Watanabe, M. A. McGuire, W. Yao, D. Xiao, K.-M. C. Fu, and X. Xu, *Science Advances* **3**, e1603113 (2017).
- [6] L. Chen, J.-H. Chung, B. Gao, T. Chen, M. B. Stone, A. I. Kolesnikov, Q. Huang, and P. Dai, *Physical Review X* **8**, 041028 (2018).
- [7] W. Jin, H. H. Kim, Z. Ye, S. Li, P. Rezaie, F. Diaz, S. Siddiq, E. Wauer, B. Yang, C. Li, S. Tian, K. Sun, H. Lei, A. W. Tsen, L. Zhao, and R. He, *Nature Communications* **9**, 5122 (2018).
- [8] L. Thiel, Z. Wang, M. A. Tschudin, D. Rohner, I. Gutiérrez-Lezama, N. Ubrig, M. Gibertini, E. Giannini, A. F. Morpurgo, and P. Maletinsky, *Science* **364**, 973 (2019).
- [9] C. Jin, Z. Tao, K. Kang, K. Watanabe, T. Taniguchi, K. F. Mak, and J. Shan, (2019), arXiv:1910.13023.
- [10] T. Song, Z. Fei, M. Yankowitz, Z. Lin, Q. Jiang, K. Hwangbo, Q. Zhang, B. Sun, T. Taniguchi, K. Watanabe, M. A. McGuire, D. Graf, T. Cao, J.-H. Chu, D. H. Cobden, C. R. Dean, D. Xiao, and X. Xu, *Nature Materials* **18**, 1298 (2019).
- [11] X. Cai, T. Song, N. P. Wilson, G. Clark, M. He, X. Zhang, T. Taniguchi, K. Watanabe, W. Yao, D. Xiao, M. A. McGuire, D. H. Cobden, and X. Xu, *Nano Letters* **19**, 3993 (2019).
- [12] W. Chen, Z. Sun, Z. Wang, L. Gu, X. Xu, S. Wu, and C. Gao, *Science* **366**, 983 (2019).
- [13] Z. Sun, Y. Yi, T. Song, G. Clark, B. Huang, Y. Shan, S. Wu, D. Huang, C. Gao, Z. Chen, M. McGuire, T. Cao, D. Xiao, W.-T. Liu, W. Yao, X. Xu, and S. Wu, *Nature* **572**, 497 (2019).
- [14] D. Zhong, K. L. Seyler, X. Linpeng, N. P. Wilson, T. Taniguchi, K. Watanabe, M. A. McGuire, K.-M. C. Fu, D. Xiao, W. Yao, and X. Xu, *Nature Nanotechnology* 10.1038/s41565-019-0629-1 (2020).
- [15] Z. Wang, I. Gutiérrez-Lezama, N. Ubrig, M. Kroner, M. Gibertini, T. Taniguchi, K. Watanabe, A. Imamoglu, E. Giannini, and A. F. Morpurgo, *Nature Communications* **9**, 2516 (2018).
- [16] T. Song, X. Cai, M. W.-Y. Tu, X. Zhang, B. Huang, N. P. Wilson, K. L. Seyler, L. Zhu, T. Taniguchi, K. Watanabe, M. A. McGuire, D. H. Cobden, D. Xiao, W. Yao, and X. Xu, *Science* **360**, 1214 (2018).
- [17] D. Ghazaryan, M. T. Greenaway, Z. Wang, V. H. Guarocho-Moreira, I. J. Vera-Marun, J. Yin, Y. Liao, S. V. Morozov, O. Kristanovski, A. I. Lichtenstein, M. I. Katsnelson, F. Withers, A. Mishchenko, L. Eaves, A. K. Geim, K. S. Novoselov, and A. Misra, *Nature Electronics* **1**, 344 (2018).
- [18] D. R. Klein, D. MacNeill, J. L. Lado, D. Soriano, E. Navarro-Moratalla, K. Watanabe, T. Taniguchi, S. Manni, P. Canfield, J. Fernández-Rossier, and P. Jarillo-Herrero, *Science* 10.1126/science.aar3617 (2018).
- [19] S. Jiang, L. Li, Z. Wang, K. F. Mak, and J. Shan, *Nature Nanotechnology* **13**, 549 (2018).
- [20] K. L. Seyler, D. Zhong, B. Huang, X. Linpeng, N. P. Wilson, T. Taniguchi, K. Watanabe, W. Yao, D. Xiao, M. A. McGuire, K.-M. C. Fu, and X. Xu, *Nano Letters* **18**, 3823 (2018).
- [21] B. Huang, G. Clark, D. R. Klein, D. MacNeill, E. Navarro-Moratalla, K. L. Seyler, N. Wilson, M. A. McGuire, D. H. Cobden, D. Xiao, W. Yao, P. Jarillo-Herrero, and X. Xu, *Nature Nanotechnology* **13**, 544 (2018).
- [22] S. Jiang, J. Shan, and K. F. Mak, *Nature Materials* **17**, 406 (2018).
- [23] M. U. Farooq and J. Hong, *npj 2D Materials and Applications* **3**, 3 (2019).
- [24] X. Xu, W. Yao, D. Xiao, and T. F. Heinz, *Nature Physics* **10**, 343 (2014).
- [25] K. F. Mak, D. Xiao, and J. Shan, *Nature Photonics* **12**, 451 (2018).
- [26] M. Onga, Y. Zhang, T. Ideue, and Y. Iwasa, *Nature Materials* **16**, 1193 (2017).
- [27] K. F. Mak, C. Lee, J. Hone, J. Shan, and T. F. Heinz, *Physical Review Letters* **105**, 136805 (2010).
- [28] S. Manzeli, D. Ovchinnikov, D. Pasquier, O. V. Yazyev, and A. Kis, *Nature Reviews Materials* **2**, 17033 (2017).
- [29] Y. Deng, Y. Yu, Y. Song, J. Zhang, N. Z. Wang, Z. Sun, Y. Yi, Y. Z. Wu, S. Wu, J. Zhu, J. Wang, X. H. Chen, and Y. Zhang, *Nature* **563**, 94 (2018).
- [30] A. K. Geim and I. V. Grigorieva, *Nature* **499**, 419 (2013).
- [31] See Supplemental Material at URL for information on the sample fabrication, experimental details, data analysis, and extended data on gate dependence, photoluminescence, and optical doping.
- [32] M. Sidler, P. Back, O. Cotlet, A. Srivastava, T. Fink, M. Kroner, E. Demler, and A. Imamoglu, *Nature Physics* **13**, 255 (2016).
- [33] K. Zollner, P. E. Faria Junior, and J. Fabian, *Physical Review B* **100**, 085128 (2019).
- [34] J. Xie, L. Jia, H. Shi, D. Yang, and M. Si, *Japanese Journal of Applied Physics* **58**, 010906 (2018).
- [35] P. Back, M. Sidler, O. Cotlet, A. Srivastava, N. Take-mura, M. Kroner, and A. Imamoglu, *Phys. Rev. Lett.* **118**, 237404 (2017).
- [36] T. Smoleński, O. Cotlet, A. Popert, P. Back, Y. Shimazaki, P. Knüppel, N. Dietler, T. Taniguchi, K. Watanabe, M. Kroner, and A. Imamoglu, *Physical Review Letters* **123**, 097403 (2019).
- [37] M. Kotani, *Journal of the Physical Society of Japan* **4**, 293 (1949).
- [38] J. F. Dillon, in *Proceedings of the Seventh Conference on Magnetism and Magnetic Materials*, edited by J. A. Osborn (Springer US, Boston, MA, 1962) pp. 1191–1192.

- [39] J. L. Lado and J. Fernández-Rossier, *2D Materials* **4**, 035002 (2017).
- [40] H. L. Davis and A. Narath, *Physical Review* **134**, A433 (1964).
- [41] E. J. Samuelsen, R. Silbergliitt, G. Shirane, and J. P. Remeika, *Physical Review B* **3**, 157 (1971).
- [42] L. de Jongh and A. Miedema, *Advances in Physics* **23**, 1 (1974).
- [43] M. E. Fisher, *Reviews of Modern Physics* **46**, 597 (1974).
- [44] See <https://doi.org/10.3929/ethz-b-000397581>.
- [45] F. J. Kopp and T. Ashworth, *Review of Scientific Instruments* **43**, 327 (1972).
- [46] L. Wang, I. Meric, P. Y. Huang, Q. Gao, Y. Gao, H. Tran, T. Taniguchi, K. Watanabe, L. M. Campos, D. A. Muller, J. Guo, P. Kim, J. Hone, K. L. Shepard, and C. R. Dean, *Science* **342**, 614 (2013).

# Supplemental Material: Observation of Magnetic Proximity Effect in Resonant Optical Spectroscopy of an Electrically Tunable $\text{MoSe}_2/\text{CrBr}_3$ Heterostructure

Livio Ciorciaro,<sup>1,\*</sup> Martin Kroner,<sup>1</sup> Kenji Watanabe,<sup>2</sup>  
Takashi Taniguchi,<sup>2</sup> and Atac Imamoglu<sup>1</sup>

<sup>1</sup>*Institut für Quantenelektronik, ETH Zürich,  
Auguste-Piccard-Hof 1, 8093 Zürich, Switzerland.*

<sup>2</sup>*National Institute for Materials Science,  
1-1 Namiki, Tsukuba 305-0044, Japan*

(Dated: December 15, 2022)

## I. SAMPLE FABRICATION

All flakes were exfoliated from crystals onto Si/SiO<sub>2</sub> substrates, and thicknesses identified by their optical contrast. The hexagonal boron-nitride (*h*-BN) crystals were provided by our collaborators at NIMS and all other crystals were purchased from HQ Graphene. The stack was assembled using a standard dry transfer technique [1] with poly(bisphenol A carbonate) and deposited onto a 0.5-mm-thick single-crystal quartz substrate. Electrodes were fabricated using standard lithography techniques.

## II. OPTICAL SETUP

A schematic of the optical setup is shown in Fig. S1. The measurements were carried out in a confocal microscope. For reflection measurements, an Exalos superluminescent LED centered at 1.631 eV (760 nm) was used, and a 1.797 eV (690 nm) laser diode and a HeNe-laser (1.959 eV, 632.8 nm) were used as pump in photoluminescence (PL) measurements (both pump lasers yielded the same signal). The measurements of the induced circular dichroism in MoSe<sub>2</sub> (Fig. 2(c) and (d) of the main text) were done with a tunable continuous wave Ti:sapphire laser detected with a photodiode. The magneto-optical Kerr effect (MOKE) measurements were done with a 2.755 eV (450 nm) laser diode and the intensity was modulated using an acousto-optic modulator for lock-in detection. Single aspheric lenses with numerical aperture (NA) of 0.7 (red light) and 0.55 (blue light) were used to focus the lasers on the sample. The two lenses were mounted simultaneously inside the cryostat on the front side (red) and back side (blue) of the sample, such that Kerr rotation and spectra could be measured by rotating the sample by 180 degrees without warming up. The Kerr rotation was measured through the substrate. To avoid effects from the birefringence of the quartz substrate, the linear polarization was chosen along a crystal axis.

## III. TEMPERATURE TUNING

In the cryostat where the measurements were done, the sample is cooled directly by a flow of helium gas in a variable temperature insert. The temperature can be tuned by heating

---

\* livioc@phys.ethz.ch



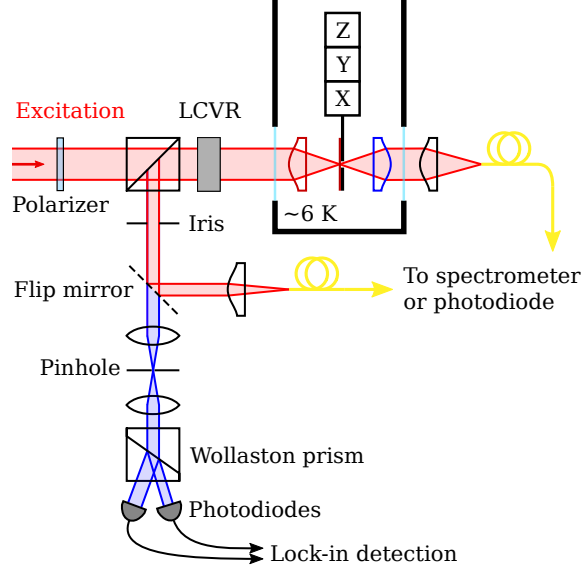


FIG. S1. Schematic of the optical setup. The circular polarization was set using a liquid crystal variable retarder (LCVR).

the helium gas at the inlet with a resistive heater. To measure the sample temperature we mounted an Allen-Bradley resistor on the sample holder at approximately the same height as the sample along the temperature gradient. Its resistance curve as a function of temperature was measured in advance using a different system with a calibrated thermometer and fitted using the three-parameter model [2]

$$\log R = A + \frac{B}{T^P}. \quad (1)$$

Differences in the resistance of the lines and a temperature gradient between the sample and the resistor may lead to systematic errors in the temperature readout. However, in the relevant range of temperatures around the critical temperature these would lead to a nearly linear shift of the temperature axis and would not affect the critical exponents significantly.

#### IV. GATE TUNING AND HBN THICKNESS

The thicknesses of the *h*-BN flakes were estimated from their colors and verified with atomic force microscopy (AFM) measurements, shown in Fig. S2. As discussed in the main text, the thickness ratio of the two *h*-BN flakes determines the voltage ratio needed between top and bottom gate to apply an electric field *E* without changing the chemical potential

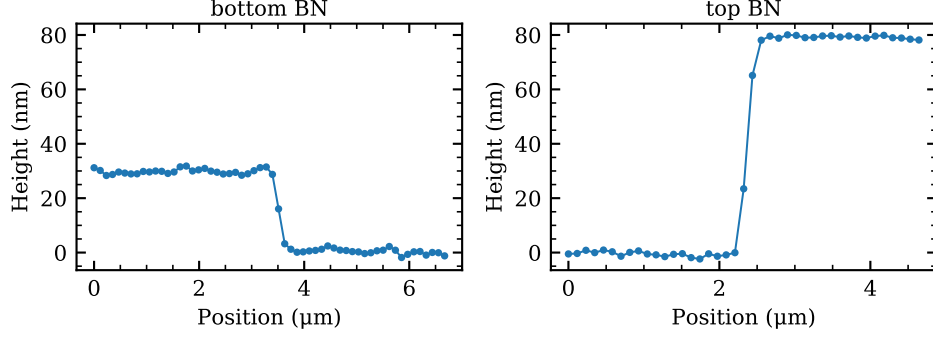


FIG. S2. Height profiles of the bottom and top hBN flakes measured with AFM.

$\mu$ . In a first approximation we consider the parallel plate capacitor formed by the top and bottom gates to be filled uniformly with a dielectric medium with relative permittivity  $\varepsilon_{\text{rel}}$ , thus neglecting the finite thicknesses of the  $\text{CrBr}_3$  bilayer and  $\text{MoSe}_2$  monolayer. Then we have  $E = (V_{\text{tg}} - V_{\text{bg}}) / (d_{\text{top}} + d_{\text{bot}})$  and  $\mu \propto d_{\text{bot}} V_{\text{tg}} + d_{\text{top}} V_{\text{bg}}$ , as defined in the main text. This means that in order to tune the electric field while keeping the chemical potential constant, the applied gate voltages need to satisfy the relation  $V_{\text{tg}} = \alpha V_{\text{bg}} + V_0$ , where  $\alpha = d_{\text{top}}/d_{\text{bot}} = 2.75$  and the offset  $V_0$  determines the chemical potential. In practice we find that the correct slope is  $\alpha = 3.3$ , by measuring a 2D sweep of top and bottom gate voltages (see Supplemental Sec. VIII) and looking at the slope of the line where the sample becomes  $p$ -doped and the exciton disappears. This discrepancy is due to the finite thicknesses and different relative permittivities of  $\text{MoSe}_2$  and  $\text{CrBr}_3$  compared to  $h$ -BN. Taking these into account the electric field is given by

$$E = \frac{V_{\text{tg}} - V_{\text{bg}}}{d_{\text{bot}} + d_{\text{top}}} \cdot \left( \frac{\varepsilon_{\text{MoSe}}}{\varepsilon_{h\text{-BN}}} + \frac{\varepsilon_{\text{MoSe}}}{\varepsilon_{\text{CrBr}}} \frac{d_{\text{CrBr}}}{d_{\text{bot}} + d_{\text{top}}} + \frac{d_{\text{MoSe}}}{d_{\text{bot}} + d_{\text{top}}} \right)^{-1}.$$

While the values will be different depending on the ratio of dielectric constants, the field is still proportional to the difference between the applied top and bottom gate voltages as long as there are no free charges in the heterostructure (between the capacitor plates), which we can verify spectroscopically.

## V. BARE $\text{CrBr}_3$ MOKE

To verify that we indeed probe the  $\text{CrBr}_3$  magnetization when measuring the MOKE of the heterostructure, we compare them to MOKE measurements of bare  $\text{CrBr}_3$ . Figures S3(a)

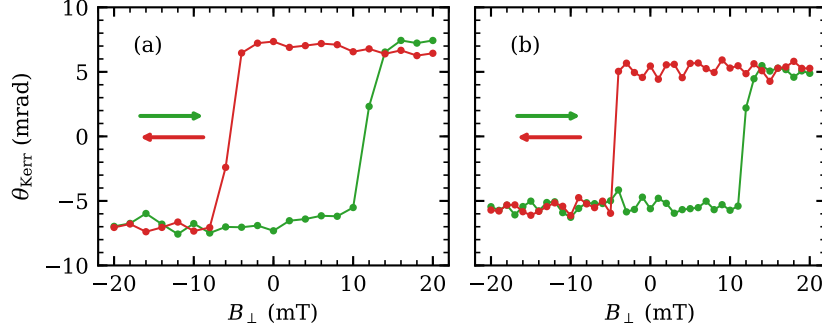


FIG. S3. MOKE measured on (a) bare  $\text{CrBr}_3$ , and (b) the heterostructure.

and (b) show the MOKE measured on bare  $\text{CrBr}_3$  and on the heterostructure, respectively. The signal is very similar, with small differences in magnitude of the rotation angle and coercive field which can be explained by sensitivity on the focus position and disorder in the sample.

## VI. PHOTOLUMINESCENCE MEASUREMENTS

As stated in the main text, we do not observe a consistent polarization splitting of the PL signal of the heterostructure. Even in photoluminescence excitation measurements under linear excitation of the exciton peak and circular detection we do not observe a splitting or any clear polarization dependence, as shown in Fig. S4(a) and (b). The sharp line that moves linearly with the excitation wavelength is a Raman peak stemming from the optical fiber. A typical PL spectrum without any polarization dependence is shown in Fig. S4(c). Near the edges of the sample some spots can be found where there is a small intensity difference between the two circular polarizations on the red tail of the broad emission peak. An example is shown in Fig. S4(d). This polarization dependence also responds to a switching of the  $\text{CrBr}_3$  magnetization. However, since we observe this behavior only on isolated spots near the edge of the flake, we do not consider it a generic feature that is relevant to our discussion.

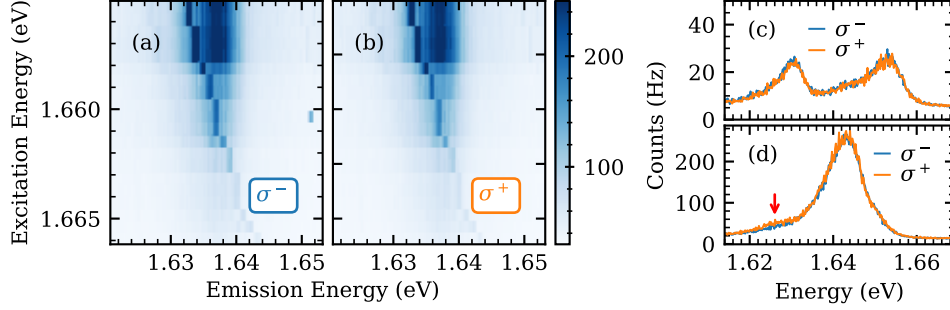


FIG. S4. (a), (b) Photoluminescence spectrum vs. excitation wavelength in  $\sigma^-$  and  $\sigma^+$  detection under linearly polarized excitation. There is no difference between the two polarizations in the detected light. The sharp peak that depends linearly on the excitation wavelength is a Raman peak from the optical fiber. (c) A typical PL spectrum of the heterostructure. There is no measurable difference between the polarizations. (d) The PL spectrum at a particular spot near the edge of the MoSe<sub>2</sub> flake shows a slight difference in emission intensity between the two circular polarizations, but no splitting.

## VII. FAST CHARGE TRANSFER: OPTICAL DOPING

In the main text we argue that the broadening of the exciton lines of the heterostructure with respect to bare MoSe<sub>2</sub> excitons as well as the weak PL signal stem from fast tunneling of electrons from the MoSe<sub>2</sub> conduction band to the CrBr<sub>3</sub> conduction band. To support this claim and to exclude that the linewidth is simply dominated by inhomogeneous broadening we show that we can optically dope MoSe<sub>2</sub> in the presence of CrBr<sub>3</sub>. For this, we measure the transmission spectrum in circular polarization at zero gate voltage while pumping the high-frequency tail of the exciton resonance with a laser in the orthogonal polarization. Transmission spectra at different pump powers are shown in Fig. S5(a). At pump powers above 30  $\mu$ W, the exciton resonance blueshifts and broadens considerably and the attractive polaron resonance emerges. This is consistent with fast non-radiative electron relaxation, leaving behind itinerant holes when the photoexcited electrons tunnel out of MoSe<sub>2</sub>, as shown schematically in Fig. S5(b). At the same pump powers on bare MoSe<sub>2</sub> we do not see the attractive polaron peak emerge. Instead, PL from the MoSe<sub>2</sub> exciton starts to dominate the spectrum as the pump power increases.

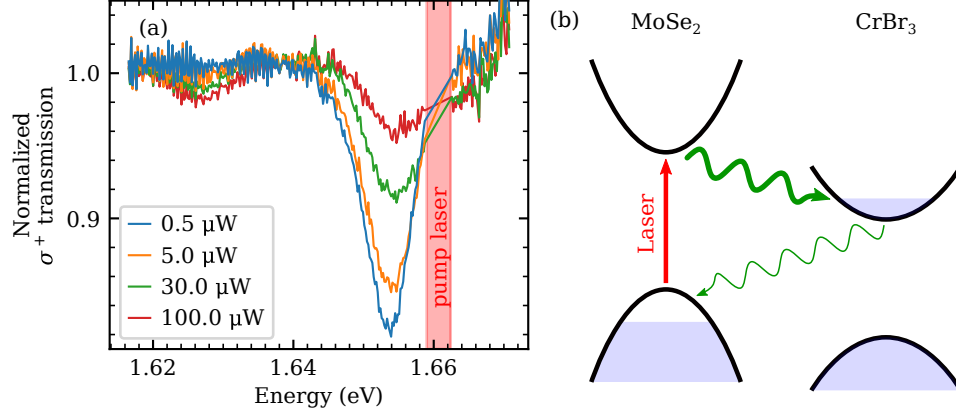


FIG. S5. (a) Transmission spectra of the heterostructure measured while pumping the exciton resonance with different powers. As the pump power increases, the exciton peak broadens and blueshifts, while the attractive polaron peak emerges, signifying that we optically dope MoSe<sub>2</sub>. (b) Schematic of relaxation dynamics in the heterostructure under laser excitation of MoSe<sub>2</sub>. Fast decay of electrons from the MoSe<sub>2</sub> conduction band into long lived states in the CrBr<sub>3</sub> conduction band lead to a dynamical equilibrium with an excess hole population in MoSe<sub>2</sub>.

### VIII. EXTENDED GATE DEPENDENCE DATA

In Fig. S6 we show the full data of reflection spectra vs. top and bottom gate voltage. Contour plots of fitted parameters of the exciton resonances as function of both gate voltages are shown in Fig. S6(a)–(c). Voltage ranges labeled *p* and *i* correspond to *p*-doped and neutral MoSe<sub>2</sub> throughout the whole heterostructure, while in the region labeled (*n*) only the bare MoSe<sub>2</sub> is *n*-doped, creating an electrical contact to the CrBr<sub>3</sub> flake and allowing it to be *n*-doped as well. The straight red lines separating the regions also represent lines of constant chemical potential (see Supplemental Sec. IV). Figure S6(a) shows the gate dependence of the center wavelength of the two exciton peaks (average of the two peak positions). The direction of the contour lines indicates that the redshift depends only on the chemical potential and we attribute this shift to a weak attractive interaction between an exciton in MoSe<sub>2</sub> and the electrons populating the CrBr<sub>3</sub> conduction band when it is charged. In Fig. S6(b) we plot the FWHM of the  $\sigma^+$ -polarized resonance. In the neutral region the contour lines indicate that the peak width depends mostly on the electric field. In the (*n*) region CrBr<sub>3</sub> becomes charged and screens the MoSe<sub>2</sub> flake from the top gate, as evidenced

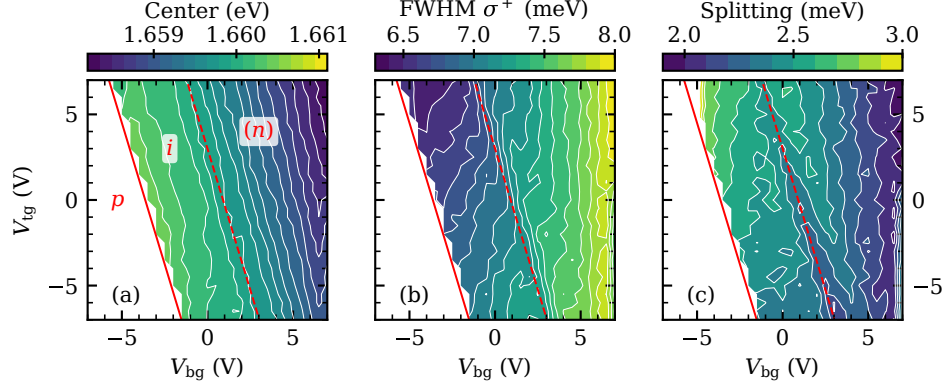


FIG. S6. (a) Contour plot of the average of the fitted exciton peak positions from circularly polarized reflection spectra of the heterostructure as function of both gate voltages. In the voltage ranges marked  $p$  and  $i$ , MoSe<sub>2</sub> is  $p$ -doped or neutral, respectively, and in the region marked  $(n)$  the bare MoSe<sub>2</sub> is  $n$ -doped, providing electrical contact to the CrBr<sub>3</sub> flake. The exciton line redshifts as the CrBr<sub>3</sub> flake becomes charged. (b) Contour plot of the fitted FWHM of the  $\sigma^+$  exciton as function of gate voltages. The peak width is sensitive only to the vertical electric field. Vertical contour lines in the  $(n)$  region indicate that the charged CrBr<sub>3</sub> flake screens the MoSe<sub>2</sub> flake from the top gate. (c) Contour plot of the fitted valley splitting as function of gate voltages. Similar to the FWHM, the splitting is affected mostly by the vertical electric field.

by the vertical orientation of the contour lines, making it impossible to independently control electric field and chemical potential. The  $\sigma^-$ -polarized resonance shows the same qualitative behavior. The splitting between the excitons also shows a similar trend as the widths, as shown in Fig. S6(c).

## IX. DATA ANALYSIS

### A. Spectroscopy

The reflection and transmission spectra were normalized by taking spectra next to the MoSe<sub>2</sub> and CrBr<sub>3</sub> flakes, but still on the stack of graphene- $h$ -BN- $h$ -BN-graphene. To reduce the sensitivity on focal drifts when moving the nanopositioners between background and data measurements, the NA of the detection path was reduced with an iris. The spatial resolution was not impaired by this as we still used the full NA in the excitation path. After



verifying that the only spectral features stem from the MoSe<sub>2</sub> exciton at charge neutrality and the attractive polaron at high hole doping, we normalized the the low- and high-energy halves of the spectra with respect to the spectra measured at a gate voltage where there is no signal in the respective energy range. This was done to avoid moving the nanopositioners between measurements and ensure to have consistent datasets from the same spot. Due to interference of the multiple reflections at the interfaces in the stack, the lines in resonant spectra have a dispersive Lorentzian shape. Therefore we use the model

$$f(x) = \Re \left( \frac{a}{\pi \sigma - i(x - x_0)} e^{-i\varphi} + c \right) \quad (2)$$

with five free parameters  $a$ ,  $c$ ,  $\varphi$ ,  $\sigma$ , and  $x_0$  to fit the spectral lineshapes. The peak center is at  $x_0$ , the FWHM is  $2\sigma$ , the peak height is  $a/(\pi\sigma)$ , and the peak area is  $a$ .

## B. Magneto-optical Kerr Effect

The MOKE was measured by sending the reflected linearly polarized light through a Wollaston prism with its optical axis rotated by 45° with respect to the polarization of the excitation beam. For small Kerr rotation angles, this leads to approximately equal intensities  $I_H$  and  $I_V$  in the two outgoing beams, which are measured using two photodiodes. The deviation from 45° polarization is then given by

$$\theta_K = \frac{1}{2} \arcsin \left( \frac{I_H - I_V}{I_H + I_V} \right) \approx \frac{1}{2} \frac{I_H - I_V}{I_H + I_V}. \quad (3)$$

## C. Critical Behavior

To obtain the magnetization and susceptibility curves as a function of temperature, we measure magnetic field sweeps of the reflection spectra in  $\sigma^-$  and  $\sigma^+$  polarization at each temperature and fit the exciton peaks to extract the splitting. Assuming that the splitting is proportional to the magnetization of CrBr<sub>3</sub>, we get the magnetization curve from the splitting at zero field and the susceptibility from the slope of the splitting at zero field. We determine the real zero magnetic field by identifying the center of the hysteresis curve or the point where the two peak positions cross above the Curie temperature, and find that it is slightly shifted to about 1 mT, probably due to some slightly ferromagnetic component in our setup. For the magnetization we use the mean splitting of the three points closest to

zero field and for the susceptibility we fit five points around zero field with a linear model to extract the slope. In both cases, this procedure may systematically underestimate the real value close to the critical temperature.

For the simultaneous fits of the magnetization and susceptibility curves, the data was normalized in order to have similar weights for all data points. Since the susceptibility was extracted from linear fits to the splitting around zero field, we have a good estimate for the error on these points that we can include as weighting factors in the fit for the critical exponents. For the magnetization data points, which correspond directly to fitted peak positions, the statistical uncertainty is very small but they are subject to systematic errors, mainly due to thermal expansion that moves the measurement spot on the sample in the temperature sweep. Both for  $T > T_C$  and  $T < T_C$  a few more data points close to  $T_C$  were measured that are not shown in Fig. 4 of the main text. These data points were excluded for three reasons: first, close to  $T_C$  it becomes more challenging to extract reliable values due to the vanishing splitting and the diverging susceptibility. Second, we are limited by the minimum step size of the magnetic field. Third, the finite sample size effects and disorder become dominant close to the phase transition. In Fig. S7 we show the full data set on a logarithmic scale, such that the power laws appear as linear dependence. For  $|T/T_C - 1| > 3 \cdot 10^{-2}$  the data points agree well with the fitted power law, but close to  $T_C$  they deviate from it, as pointed out above. Additionally, we show the measured magnetization divided by the applied magnetic field for all data points above the critical temperature in Fig. S7(b), which also follows the same power law.

- 
- [1] L. Wang, I. Meric, P. Y. Huang, Q. Gao, Y. Gao, H. Tran, T. Taniguchi, K. Watanabe, L. M. Campos, D. A. Muller, J. Guo, P. Kim, J. Hone, K. L. Shepard, and C. R. Dean, *Science* **342**, 614 (2013).
  - [2] F. J. Kopp and T. Ashworth, *Review of Scientific Instruments* **43**, 327 (1972).

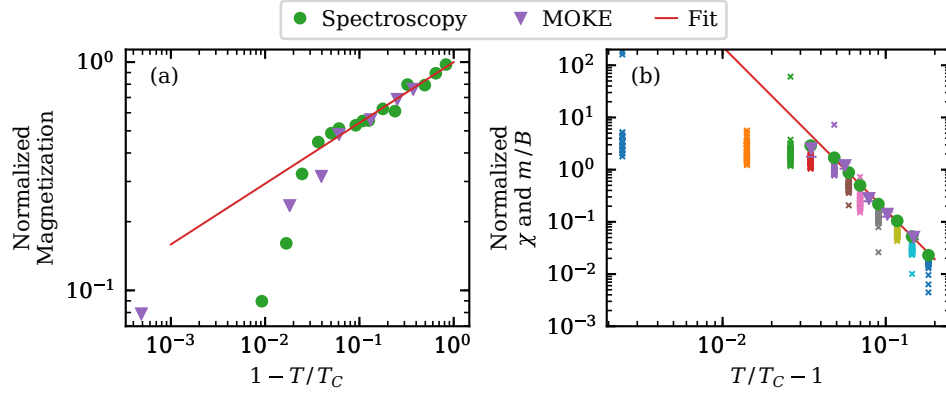


FIG. S7. (a) Normalized remnant magnetization as function of temperature and (b) normalized susceptibility as function of temperature. Solid lines, filled circles and filled triangles are the same as shown in the main text; crosses are  $m/B$  from individual data points. In both cases the data points follow the fitted power law when  $|T/T_C - 1| > 3 \cdot 10^{-2}$ .